Plasma Sources
Science and
Technology

PURPOSE-LED
PUBLISHING™

Mass utilization scaling with propellant type on a magnetically shielded Hall thruster

To cite this article: W J Hurley and B A Jorns 2025 *Plasma Sources Sci. Technol.* **34** 055010

OPEN ACCESS
IOP Publishing
Plasma Sources Science and Technology
Plasma Sources Sci. Technol. **34** (2025) 055010 (14pp)
https://doi.org/10.1088/1361-6595/add61e

Mass utilization scaling with propellant type on a magnetically shielded Hall thruster

W J Hurley[*] and **B A Jorns**

Department of Aerospace Engineering, University of Michigan, 1320 Beal Avenue, Ann Arbor, MI
48109-2140, United States of America

E-mail: wjhurley@umich.edu

Received 21 October 2024, revised 21 April 2025
Accepted for publication 8 May 2025
Published 23 May 2025

Abstract

An analytical model for Hall thruster ionization efficiency on multiple propellants is derived and validated with experimental data. The experimental dataset includes previous results from a magnetically shielded Hall thruster operating on xenon and krypton over a wide discharge current range (Su *et al* 2024 *J. Propl. Power* **40** 661–800) and new experimental results with the same thruster on argon and nitrogen. The analytical model is derived by integrating the neutral continuity equation along the length of the thruster channel. A series of scaling laws is then used to relate this model to key global operating characteristics of the thruster. The results indicate that with a learned characteristic channel length for the entire data set, the model accurately captures mass utilization trends as a function of a single parameter for all four propellants. The extensibility of the model beyond the range of experimental data is explored, and it is found that the dependence of the mass utilization on discharge voltage is consistent with the scaling exhibited by previously studied Hall thrusters.

Keywords: electric propulsion, Hall thrusters, alternative propellants, ionization scaling

1. Introduction

Hall thrusters, the most flown electric propulsion devices, are widely used for satellite station keeping, orbit raising, and deep space robotic missions. These quasi-neutral, axisymmetric devices utilize orthogonal electric and magnetic fields to ionize and accelerate a neutral gas to produce thrust. Any non-ionized neutrals represent a loss in possible thrust and thus a decrease in overall device efficiency. To ensure most of the propellant is ionized, Hall thrusters are designed so that the mean free path of ionization for neutral gas is much less than the thruster channel length. Following this criterion, optimally designed Hall thrusters ionize the majority ($\geqslant$90 %) of the input propellant [1].

Historically, many Hall thrusters have been optimized for xenon propellant. Xenon is widely used because it stores densely, has a large ionization cross section, and has a high atomic mass—resulting in high thrust-to-power ratios. While xenon has many desirable properties, it is an extremely rare gas in the Earth's atmosphere, which makes it expensive and subject to large price fluctuations. These attributes can be prohibitive for large scale constellations or deep space missions where substantial propellant quantities are required. For example, larger geosynchronous orbit satellites could use $>$ 50 000 L of xenon ($>$\$3 million USD in 2024) in transit, which makes propellant both expensive and difficult to stockpile [2, 3]. Some

---

[*] Author to whom any correspondence should be addressed.

missions, like nuclear electric propulsion for crewed Mars transfers, may even need more than 250 000 kg of xenon, which is more than 3 times the world annual supply in 2023 [2, 4].

Given these difficulties with xenon procurement, gases like krypton, argon, and nitrogen are increasingly being explored as substitutes. Krypton and argon are more available noble gases and are now widely used in SpaceX's Starlink constellation [5]. Molecular gases like nitrogen could be harvested in-situ for drag compensation of very low earth orbit satellites [6]. Although alternative propellants present numerous advantages at a systems level, the high performance of Hall thrusters designed to operate on xenon does not typically extend to alternative gasses [7, 8]. This historically, in large part, has been attributed to their faster thermal velocities and smaller ionization cross sections than xenon, which translate to a reduced probability of ionization in the thruster.

Since the propellant utilization is heavily intertwined with the overall device performance, there is a pressing need to develop improved, first-principles informed universal scaling laws for the physical mechanisms that drive this process for disparate gases. A number of simple models have been developed to date to describe the ionization process in Hall thrusters [8–11]. Recently, Su *et al* [11] proposed a simplified 0D scaling law for the dependence of mass utilization on the operating conditions of a thruster running with xenon and krypton. The goal of this work is to expand on this model, improving its fidelity and broadening the data set to include operating conditions with multiple discharge voltages and a wide range of discharge currents for argon and nitrogen.

This paper is organized in the following way. In section 2, we outline our updated scaling law for the mass utilization efficiency. Then, in sections 3 and 4, we provide an overview of the experimental setup and analysis techniques to infer the mass utilization efficiency and outline the key assumptions for our model. We next compare the model predictions to experimental data in section 5, followed by a discussion of the key results in section 6.

2. Scaling law for mass utilization

In this section, we introduce a simplified scaling law for the mass utilization efficiency. This derivation is largely based on the previous work by Su *et al* [11] with modifications to accommodate additional propellants.

We show in figure 1(a) a canonical representation of the Hall thruster principle of operation. In this axisymmetric device, a potential difference, V_D, is applied between the positive anode and negative cathode. The hollow cathode thermionically emits electrons that are pulled into the thruster channel with a coupling potential, V_cc. They are then impeded on their path to the anode by the radial magnetic field. These electrons gyrate around field lines and drift azimuthally due to the perpendicular electric and magnetic fields. The drifting electrons collide with and ionize the majority of neutral gas in the 'ionization region,' shown in figure 1(b) with characteristic length, L_iz. These newly created ions are unmagnetized due to their large mass and are accelerated downstream by a potential drop, $V_\mathrm{acc} = V_\mathrm{D} - V_\mathrm{cc}$, to produce thrust. This region of large potential decrease with characteristic length, L_acc, is referred to as the 'acceleration region.' We note here that propellant ionization does not occur uniformly through the thruster channel, and there are regions, such as near the anode, in which it is negligible [1]. Therefore, the length scale relevant to ionization $\bar{L}$ may be smaller than the channel length, L_ch.

In a Hall thruster, it is common to quantify the degree of ionization of the propellant with the mass utilization:

$$\eta_m = 1 - \frac{\dot{m}_\mathrm{n}\left(L_\mathrm{ch}\right)}{\dot{m}_\mathrm{n}\left(0\right)} = 1 - \frac{n_\mathrm{n}\left(L_\mathrm{ch}\right)}{n_\mathrm{n}\left(0\right)}. \tag{1}$$

In this expression, $\dot{m}_\mathrm{n}(0)$ is the neutral mass flow rate at the anode ($x = 0$), and $\dot{m}_\mathrm{n}(L_\mathrm{ch})$ is the neutral mass flow rate at the channel exit ($x = L_\mathrm{ch}$). We have assumed here that the neutral thermal velocity, channel area, and average neutral mass remain constant along the channel length so that the ratio of mass flow rates can be written in terms of number density, n_n. Intuitively, this equation indicates that if no neutrals remain at the channel exit (all are ionized), the mass utilization is unity. We note here that other common definitions of mass utilization choose to incorporate the cathode flow, which in principle can be ionized and contribute to the beam. However, in this analysis we focus on the discharge channel and neglect this contribution.

To relate the mass utilization to key aspects of the thruster operation, we motivate an analytical expression for the ratio of the exit and inlet neutral densities. We find this from a consideration of the 1-D, steady-state, neutral continuity equation:

$$v_n \frac{\mathrm{d}n_\mathrm{n}}{\mathrm{d}x} = -n_\mathrm{n} n_\mathrm{e} k_\mathrm{iz}\left(T_\mathrm{e}\right), \tag{2}$$

where v_n is the neutral velocity, n_e is the electron number density, and $k_\mathrm{iz}(T_\mathrm{e})$ is the total ionization rate coefficient averaged over a 1D Maxwellian electron population with temperature T_e. We define the neutral thermal velocity as $v_\mathrm{n} = \sqrt{\frac{2k_\mathrm{b}T_\mathrm{n}}{\pi m}}$, where T_n is the neutral gas temperature, k_b is the Boltzmann constant, and m is the neutral mass [12]. Next, we integrate this expression from the anode ($x = 0$) to the end of the channel ($x = L_\mathrm{ch}$) and combine the result with equation (1) to yield

$$\eta_\mathrm{m} = 1 - \exp\left[-\frac{\langle n_\mathrm{e} k_\mathrm{iz}\left(T_\mathrm{e}\right)\rangle}{v_\mathrm{n}} \bar{L}\right]. \tag{3}$$

Here we have denoted $\bar{L}$ as the characteristic region in the channel where ionization is non-negligible. This does not necessarily equal the full channel length, i.e. $\bar{L} < L_\mathrm{ch}$. The quantity $\langle\rangle$ denotes the average of the indicated properties over the region $\bar{L}$. Equation (3) highlights the key parameters that impact the mass utilization efficiency. Notably, longer characteristic lengths, denser plasmas, and higher ionization rates promote a larger ionization fraction while faster thermal velocities lower ionization.

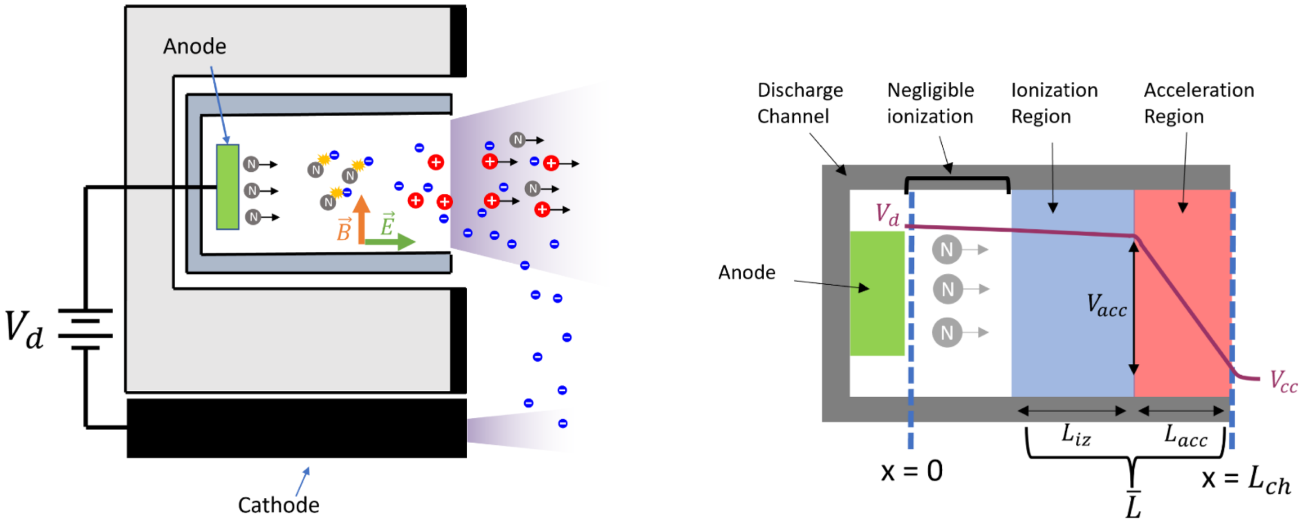

(a) (b)

Figure 1. (a) Cross section of a Hall thruster channel illustrating the principle of operation. (b) Zoomed in view of the discharge channel region.

Now that we have introduced our mass utilization formulation in terms of plasma properties, we attempt to relate these to global properties of the thruster operation, e.g. discharge voltage and current. To that end, for the density, we leverage the generalized Ohm's law where we neglect the pressure contributions to find

$$n_e = \frac{j_e B^2}{E m_e \nu_c}, \tag{4}$$

where j_e is the electron current density, E is the electric field, $B$is the magnetic field, m_e is the electron mass, and ν_c is the electron collision frequency.

To use equation (4) to solve for the electron density, we need a way to estimate the electron collision frequency. However, it has been well established that the collision frequency derived from classical elastic and inelastic collisions of electrons with other particles does not capture the observed electron transport in these devices. Indeed, the exact form of ν_c is still an active area of investigation in the Hall thruster community [13–17]. Given the lack of a first principles model for ν_c, we adopt a common approach for these devices that has been shown to improve the fidelity of representing the electron dynamics [13–15, 18–20]. This is based on assuming the collision frequency scales with the electron cyclotron frequency:

$$\nu_c = \alpha \omega_e, \tag{5}$$

where $\omega_e = qB/m_e$ is the electron cyclotron frequency, q is the fundamental charge, and α is a constant on the order 10^{-2} – 10^{-3} [14, 16]. We next represent electron current density in terms of total discharge with

$$j_e = j_D (1 - \eta_b), \tag{6}$$

where A is the channel area, η_b is the beam utilization efficiency, and j_D is the discharge current density or ratio between discharge current and channel area. The beam utilization efficiency is defined as the ratio between ion beam current I_b and discharge current I_d:

$$\eta_b = \frac{I_b}{I_d}. \tag{7}$$

Finally, for the electric field in equation (4), we employ the linearization

$$E = V_{acc}/L_{acc}. \tag{8}$$

Leveraging equations (3)–(8), we now can express the mass utilization as

$$\eta_m = 1 - \exp\left(-\frac{\bar{L}}{\lambda_i}\right), \tag{9}$$

where we have introduced the parameter λ_i defined as

$$\lambda_i = \sqrt{\frac{2 T_n k_b}{\pi m_i}} \frac{(V_{acc}) \alpha q}{L_{acc} B (1 - \eta_b) \langle k_{iz} (T_e) \rangle j_D}. \tag{10}$$

Physically, λ_i represents the mean free path for ionization, and according to this simplified theory will universally predict the mass utilization efficiency at all operating conditions on each gas. Indeed, a key feature of this result is that provided the scaling length, $\bar{L}$, is approximately constant, the mass utilization of any gas or operating condition, when expressed in terms of this effective ionization length, should collapse onto a single curve. To evaluate this in practice, we consider in the following section experimental data generated parametrically over four different gases and a range of operating conditions.

3. Experimental setup

In this section, we outline the experimental setup used to generate the mass utilization data we leveraged in this investigation. We outline the setup with descriptions of the thruster configuration, operating conditions, facility, and diagnostics.

3.1. Thruster configuration

In this campaign, we utilized a modified version of the H9 Hall thruster. This device is a 9 kW class Hall thruster previously developed through a collaboration between the Jet Propulsion Laboratory, the University of Michigan, and the Air Force Research Laboratory [21, 22]. It employs a magnetically-shielded topography where the magnetic field is tailored to reduce erosion of the channel walls [23, 24]. The H9 has been extensively characterized on both xenon and krypton and shares design features with the advanced electric propulsion system [25].

The version of the H9 we utilized in this work is based on the modified version described in [26]. Key elements include a graphite discharge chamber, water-cooled magnetic bobbins, and a centrally mounted hollow LaB6 cathode.

Electrically, the thruster body was grounded for most experimental configurations with a few exceptions where the body was electrically tied to the cathode. We believe this configuration difference had a minimal impact on the results given the past studies of [27]. The magnetic field magnitude was tailored to be consistent with the previous parametric study on the H9 [11].

3.2. Operating conditions

Table 1 shows the range of operating conditions and propellants for which we experimentally measured the mass utilization. We note here that for both xenon and krypton, we leveraged an existing dataset from the work of Su *et al* in which the mass utilization of krypton and xenon were experimentally characterized as a function of discharge current [11]. We have re-processed this data, however, with an updated and higher fidelity $E\times B$ analysis procedure detailed in section 4.

For this study, we expanded on the operating envelope of previous work to include parametric studies on both argon and nitrogen across a range of discharge current densities. On nitrogen, we kept the discharge voltage fixed at $V_\mathrm{D} = 300$ V, and on argon, we operated at both $V_\mathrm{D} = 200\ V$ and $V_\mathrm{D} = 300$ V. At each new condition, we set the discharge voltage and varied the mass flow rate to both the anode and cathode until we achieved a target discharge current. Alicat mass flow controllers calibrated with a Bios Defender 510 L were used to control the flow rate to the thruster to within 1% target value. We incorporate this flow rate uncertainty into our estimate of the mass utilization at each operation condition. We operated the cathode at a constant 7% particle flow fraction of the anode. In tests where the main discharge was operating on nitrogen, we utilized krypton gas for the cathode to avoid poisoning [28]. Once the mean discharge current reached a constant value, we utilized a suite of far-field probes to experimentally infer the mass utilization.

3.3. Facility

In this work as well as for the data extracted from Su *et al* [11] we operated the thruster in the Alec D. Gallimore Large Vacuum Test Facility (LVTF) at the University of Michigan. Figure 2 shows a top-down view of the experimental setup. This chamber is 6 m × 9 m and employs 12 shrouded TMI-1200i and 5 nude cryosails. The cryosails were specifically designed to pump xenon and krypton at 35–40 K and therefore are too warm to effectively capture argon or nitrogen [29]. As a result, we utilized only the 12 shrouded pumps for this work. To measure the background pressure, we mounted an IGM401 ‘Hornet’ hot cathode ionization gauge to the facility wall. The operating pressure range for each propellant is shown in table 1. Although fewer pumps were utilized when testing argon and nitrogen, the reported background pressures are comparable. The largest outlier is the maximum pressure condition with argon propellant, which is ∼25% higher than the other high-pressure conditions. For the thruster used in this analysis, this difference in pressure between argon and the other gases results in a small change in the neutral ingestion ($< 1\%$ of the total flow rate). Furthermore, using the techniques outlined in section 4, we are able to largely correct for any pressure-related differences in the probe data. As a result, the changing facility configuration and thus background pressure likely has a small impact on the final results.

As shown in figure 2, during operation, we oriented the thruster plume downstream facing the far-field probes. The Faraday probe was ∼10 thruster outer diameters downstream (D_T), and the $E\times B$ probe and Langmuir probe were 12.5 D_T downstream. These locations are in the far-field of the thruster and consistent with previous work in [11].

3.4. Diagnostics

To experimentally infer the mass utilization and provide estimates for key quantities of interest in our mass utilization model, we utilized a far-field probe suite consisting of a Faraday probe, E×B probe, and Langmuir probe. Table 2 provides a summary of the probes and inferred quantities.

The guarded, 2.38 cm diameter molybdenum Faraday probe was mounted on a probe arm and swept at a constant radius to collect ion saturation current as a function of angle with respect to thruster centerline. The arm was rotated from 0–180° and back, where 90° is defined as the thruster centerline. We then used this trace to infer the ion beam current. We biased both the collector and guard ring to −30 V to collect ion saturation current. The $E\times B$ probe, which measures the spread of ion velocities in the plume, imposed a magnetic field of 0.16 T between two electrodes spaced 0.97 cm apart. The $E\times B$ probe had an entrance collimator with an aperture of 1.6 mm and a length of 7.5 cm and an exit collimator that was 15 cm long. We swept the plate potential $V_{E\times B}$ from 0 to 150 V to capture ion species of different velocities at a single point on thruster centerline. With this information, we infer the current

Table 1. List of the discharge voltages, normalized flow rate range, and operating pressures for each gas.

Gas	Discharge voltage (V)	Anode flow rate range	Pressure (μTorr)	Data source
Argon	300	1–6.43×	9.8–42.0	This Work
Argon	200	1–5.95×	6.3–30.5	This Work
Nitrogen	300	1–4.78×	8.1–31.8	This Work
Xenon	300	1–4.48×	5.7–23.6	[11]
Krypton	300	1–5.99×	5.9–31.8	[11]

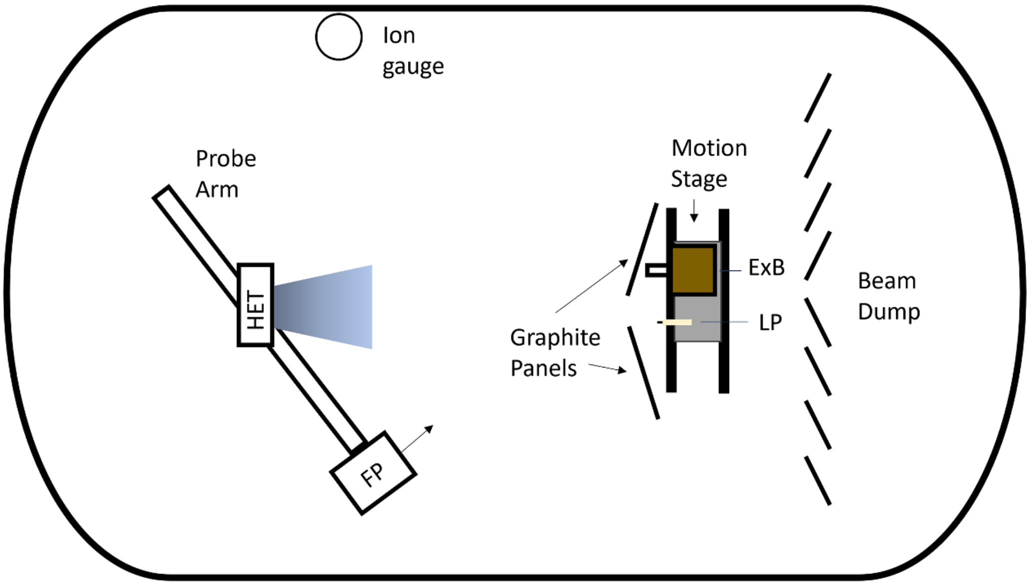

Figure 2. Top-down view of the experimental setup in LVTF. Included are the positions of the thruster, Faraday probe on the azimuthal arm, wall mounted ion gauge, and $E\times B$/Langmuir Probe on a far-field motion stage.

Table 2. List of the far-field probes and their measured quantities.

Probe	Measured quantity	Inferred property
Faraday probe	Ion saturation current	$I_\mathrm{b} \rightarrow \eta_\mathrm{b}, \eta_\mathrm{m}$
$E\times B$ probe	Ion velocity distribution	$\Omega_\mathrm{s} \rightarrow \eta_\mathrm{m}$
Langmuir probe	I–V trace	$V_\mathrm{p} \rightarrow V_\mathrm{cc}$

fractions (Ω_s) from the $E \times$ B spectra. A cylindrical 1 mm diameter by 4 mm length Langmuir probe, was used to generate an I–V trace in the plume. From this I–V trace, we inferred the plasma potential, V_p. The plasma potential was used to calculate the cathode coupling voltage V_cc. The Langmuir probe, similar to the $E \times B$, provided a single trace on thruster centerline. We followed the recommended Langmuir probe analysis procedure outlined in [30] to estimate this quantity.

4. Analysis

In this section, we discuss our analysis techniques to infer the key plume properties for experimentally estimating the mass utilization efficiency. We then outline our process for regressing our proposed model, outlined in section 2, against our parametric measurements of mass utilization.

4.1. Experimentally measuring mass utilization

We can use far-field plume measured quantities to experimentally estimate the mass utilization efficiency as

$$\eta_\mathrm{m} = \frac{\dot{m}_\mathrm{i}}{\dot{m}_\mathrm{a}} = \frac{I_\mathrm{b}}{\dot{m}_\mathrm{a}} \sum \frac{\Omega_\mathrm{s} m_\mathrm{s}}{q_\mathrm{s}}, \tag{11}$$

where $\dot{m}_a$ is the anode mass flow rate (denoted $\dot{m}_n(0)$ in equation (1)), $\dot{m}_i$ is the ion mass flow rate, and the subscript 's' denotes species-specific quantities. Equation (11) highlights

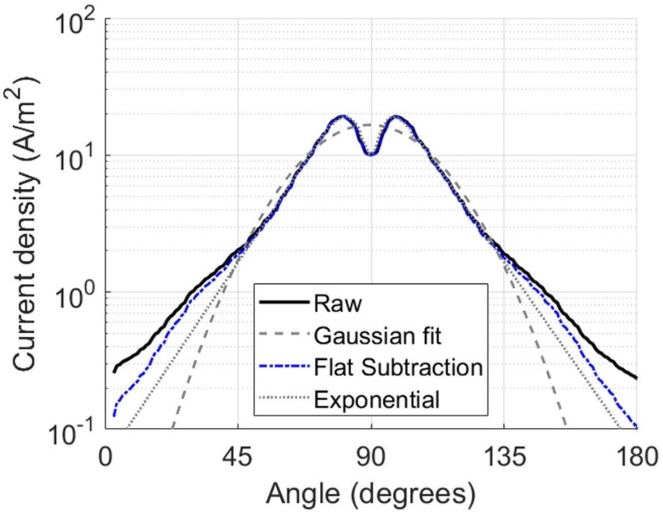

Figure 3. Ion current density profile of the H9 Hall thruster operating on argon gas with the different charge exchange correction methods plotted.

that if we can measure the total ion beam current and the fraction of current carried by each species, we can estimate the ion mass flow rate and thus mass utilization efficiency. In the following sections, we outline the analysis process to estimate these parameters and quantify their uncertainty.

4.1.1. Ion beam current. We can estimate the beam current I_b in the field-field at location R with the integral

$$I_b = 2\pi R^2 \int_0^{\pi/2} j_i(\phi)\cos\phi\,\mathrm{d}\phi, \tag{12}$$

where $j_i(\phi)$ denotes the local ion current density as a function of angle. We can estimate this current density from the Faraday probe's local measurement of ion saturation current, $I_{FP}(\phi)$, with the relationship:

$$j_i(\phi) = \frac{I_{FP}(\phi)}{A_C + \kappa_G}\kappa_{SEE}. \tag{13}$$

Here A_c is the collector area, κ_G is a correction factor for additional ions collected in the gap between the collector and guard ring, and κ_{SEE} is a correction factor due to ion impact secondary electron emission (SEE) [31]. The SEE yield, γ_i, is defined as the number of electrons liberated from a surface for an incident species. The formulas for each of these correction factors are listed in the appendix.

Figure 3 shows an example of a corrected Faraday trace of the thruster operating on argon. Physically, we see that the current density is peaked near the thruster centerline (90°) with a dip in the center due to the annular discharge. The current density decreases precipitously near the wings (oblique angles) as the Hall thruster, by design, has a primarily axial beam to ensure maximum thrust generation.

We note here that, in practice, the ion current density measurement is not a direct representation of the ion beam current. There are other contributions that can arise from the presence of charge exchange (CEX) ions. CEX ions are produced when some of the high-velocity beam ions inelastically collide and swap charge with a slow neutral particle arising from finite background pressure in the facility. The resulting ions are slow-moving and scattered at wide angles, manifesting as an artificial increase in current on the Faraday probe at oblique angles in the trace. The best method to correct for CEX ions is to take Faraday traces at multiple background pressures and then extrapolate to vacuum conditions [31]. For this analysis, we only had a single Faraday trace at each operation condition. Therefore, we adopted three standard de-convolution methods that attempt to remove CEX ions from the current density measurement. We show in figure 3 each method: a Gaussian fit [26], exponential fit [32], and a flat subtraction [33].

For the Gaussian CEX correction, a Gaussian is fit to the trace. The exponential fit is performed by curve fitting the section between ∼15°–35° off centerline (90°) in log space, and extrapolating to the wings. The flat subtraction method assumes the current density at the wings is only due to CEX ions, and therefore subtracts this value from the entire trace. We parse each segment of the Faraday probe sweep 0°–90°, 90°–180° and back into four unique estimates of the beam current. We perform all three CEX fits to each of the four segments, integrate the current density trace, and then average the results for our estimate of the beam current. We estimate the uncertainty as twice the standard deviation of the data set.

4.1.2. Current fractions. We utilize the trace generated by the $E\times B$ probe to estimate the current carried by each species in the beam of a given charge-to-mass ratio. This diagnostic operates on the principle of applying a discriminating voltage, which can be shown to be proportional to the velocity of the incoming ions, $V_{E\times B} \propto v_s = \sqrt{\frac{2q_s V_{acc}}{m_i}}$. Figure 4 shows examples of typical $E\times B$ traces, $f_{E\times B}(V_{E\times B})$, as a function of discriminating voltage for two operating conditions with xenon propellant.

In figure 4(a), we see two distinct peaks corresponding, in this case, to the first and second charge states. In principle, this raw trace can be represented as a summation of distribution functions for each charge state, $f_{E\times B}(V_{E\times B}) = \sum_s f_s(V_{E\times B})$. If we can de-convolve these from the trace, we can infer the current fractions necessary for correcting the inferred mass utilization (equation (11)) with the following:

$$\Omega_s = \frac{\int \frac{q_s}{m_s}\frac{f_s(V_{E\times B})}{V_{E\times B}^2}\mathrm{d}V_{E\times B}}{\sum_k \int \frac{q_k}{m_k}\frac{f_k(V_{E\times B})}{V_{E\times B}^2}\mathrm{d}V_{E\times B}}. \tag{14}$$

In practice, the individual distributions of charge states, as detailed by Huang *et al* [34] are estimated by assuming a form of ion velocity distribution and fitting to each peak sequentially in the $E\times B$ trace. This fitting method has historically performed well for estimating the current fractions when each peak is distinct, but it loses fidelity when the $E\times B$ trace has overlapping species distributions (see figure 4(b)). Previous analysis by Huang *et al* has suggested using saddle points and peak heights in spectra like these to estimate the maximum

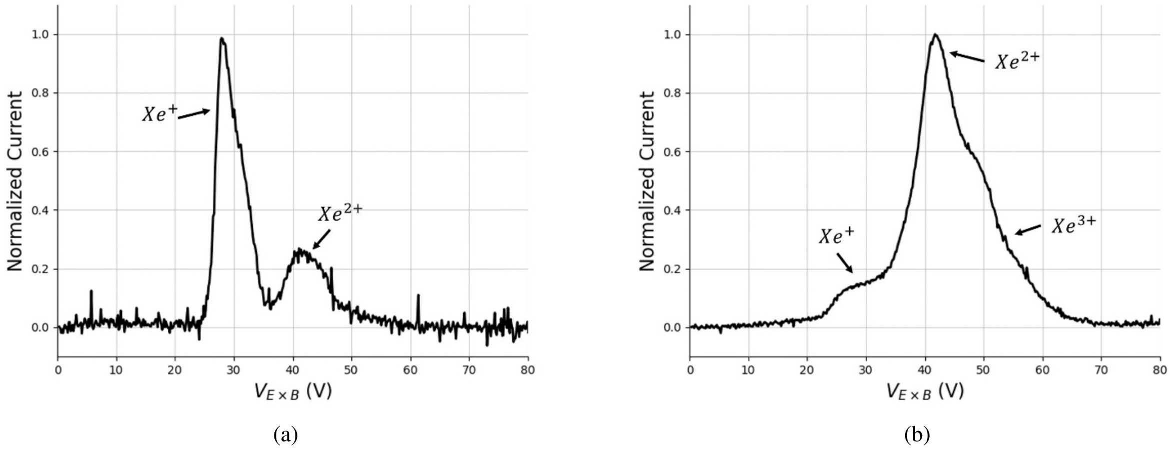

Figure 4. E×B spectra of the H9 thruster operating on xenon at (a) $V_\mathrm{d} = 300$ V, $I_\mathrm{d} = 15$ A and (b)$V_\mathrm{d} = 300$ V, $I_\mathrm{d} = 100$ A.

amount of distribution overlap and provide a 'rough approximation' of current fraction uncertainty [34]. We note here, however, that while this method can provide an upper bound in the uncertainty, it fails to provide an estimate when the locations of saddle points are ambiguous, i.e. figure 4(b).

As an attempt to rigorously account for uncertainty in convolved $E\times B$ traces, we employ Bayesian inference to learn the probabilistic distribution for each parameter of an analytic model to the data. Consistent with Huang *et al* [34], we adopt a model for the trace based on assuming each species is normally distributed:

$$f_{E\times B} = \sum_\mathrm{s} A_\mathrm{s} \exp\left(\frac{\left(V_{E\times B} - \mu_\mathrm{s}\right)^2}{\sigma_\mathrm{s}^2}\right), \tag{15}$$

where we have introduced the fitting modeling parameters of μ_s as the mean velocity of species s, σ_s as the width of the distribution, and A_s as the intensity. We learn the distribution for each of these model parameters, after introducing the experimental data d, per Bayes rule:

$$P(\theta|d) \propto P(d|\theta)P(\theta), \tag{16}$$

where $P(\theta|d)$ is a probabilistic distribution of the model parameters, $\theta = (\mu_\mathrm{s}, \sigma_\mathrm{s}, A_\mathrm{s})$ that is conditioned on the ExB data, d, $P(d|\theta)$ is the likelihood function (assumed to be normally distributed in our work), and $P(\theta)$ is an assumed prior probability distribution of the model parameters.

For the parameter A_s, we assume a uniform prior, $P(A_\mathrm{s}) = U(0,1)$. This range accounts for the fact that we normalize the $E\times B$ data based on the maximum experimental value. For the variance, σ_s, we also assume a uniform prior $P(\sigma_\mathrm{s}) = U(1,20)$. These bounds are based on inspection of the data. For the prior distribution of the mean velocity, μ_s, we assume it is distributed normally, $P(\mu_\mathrm{s}) = N(V_{E\times B(s)}, 5)$. The mean here is given by

$$V_{E\times B(s)} = B_{E\times B} w v_\mathrm{s}, \tag{17}$$

where v_s is the velocity of incoming species s, $B_{E\times B}$ is the magnetic field, and w is width between the $E \times B$ electrodes. As a first-order estimate, in this formulation, we assume that the ion velocity at the probe is due to the fall through a potential drop equal to the difference between the discharge voltage and cathode coupling voltage, $v_\mathrm{s} = \left(\frac{2q_\mathrm{s}(V_\mathrm{d} - V_\mathrm{cc})}{m_\mathrm{s}}\right)^{1/2}$. For the variance in the assumed prior distribution, we assume 5 V, which accounts for the possibility that the mean ion velocity may differ from equation (17) due to incomplete acceleration.

Since our model is non-linear, we cannot analytically solve Bayes' rule for the posterior distribution in equation (16). Therefore, we utilize Markov chain Monte Carlo to sample from the un-normalized posterior, which is the product of the likelihood (model) and prior distributions. We take the mean of the samples for each parameter in equation (15) to be our estimate. Following this procedure, we show in figure 5 an example fit to the $E\times B$ spectra of figure 4(b), where we have assumed the spectra is made up of three Gaussian's corresponding to each ion charge state. In figure 4(b) the blue bounds represent 95% credible intervals. As can be seen, the experimental data falls within the uncertainty, indicating a high-quality fit.

To estimate the current fractions, we integrate each sample for the parameters of equation (15) with equation (14). We then take the sample mean and standard deviation of the resulting data set to be our best estimate of the current fractions and uncertainties. We note here that since we utilized this new fitting method to calculate current fractions, the resulting mass utilization for xenon and krypton is ∼2%–5% different than presented in [11]. With that being said, the calculated uncertainty in the mass utilization reported in this analysis does capture the reported values of [11].

Due to CEX of the thruster plume with background neutrals, the current fractions yielded by the preceding analysis from the $E\times B$ probe are different than those leaving the thruster. To correct for the CEX attenuation, we follow a similar analysis to that first presented by Shastry *et al* [35] and modify the current density for each species as

$$\left(j_{E\times B}/j\right)_\mathrm{s} = \exp\left(-n_0\sigma_s z\right), \tag{18}$$

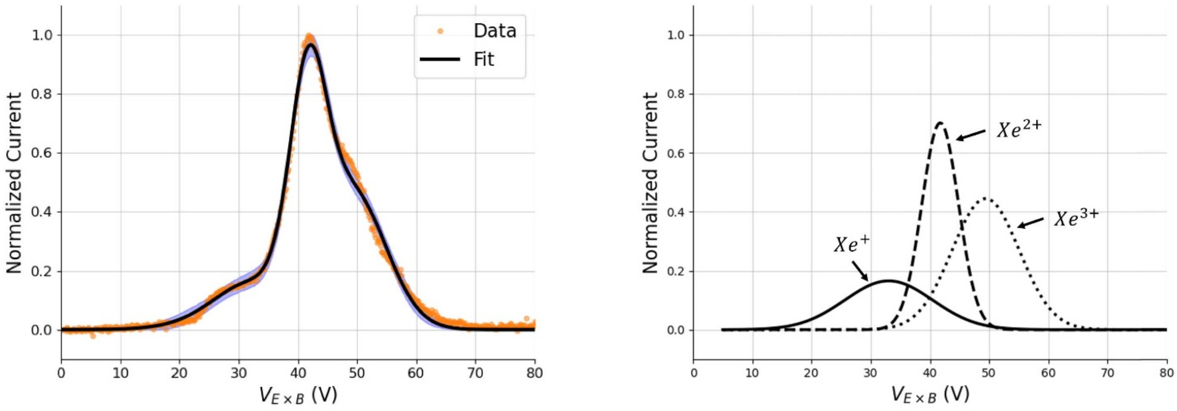

(a)

(b)

Figure 5. (a) The $E{\times}B$ spectra fit with 95% credible intervals plotted in blue, and (b) the underlying distributions of each species.

where j is the current density at the thruster exit, $j_{E\times B}$ is the current density at the $E\times B$ probe, z is axial distance of the $E\times B$ probe from the thruster, n_0 is the neutral density, and σ_s is the CEX collision cross section (provided in [36–38]). We then use this result to correct the current fractions as

$$\Omega_\mathrm{s}^{C}=\frac{\Omega_\mathrm{s}\left(j_{E\times B}/j\right)_\mathrm{s}^{-1}}{\sum_k\Omega_k\left(j_{E\times B}/j\right)_k^{-1}},\qquad(19)$$

where $\Omega_\mathrm{s}^{\mathrm{C}}$ are the corrected current fractions. We use the background pressure P_b to estimate the neutral density $n_0=P_\mathrm{b}/k_\mathrm{b}/T_\mathrm{g}$ in this relation, where we assume the gas is at room temperature $T_\mathrm{g}=300K$. The uncertainty in the CEX correction is largely driven by error in the background pressure estimate, which is ∼20% for the ionization gauge we utilized. Following [34], we apply standard error propagation methods, based on taking the partial derivative of equations (18) and (19) with respect to the neutral density, to account for the dependence of the current fractions on the uncertainty in background pressure. We then combine this result in quadrature with the uncertainty in the raw current fractions.

4.2. Model assumptions

In this section, we describe the key model assumptions and calibration procedures we employed in this analysis. We begin by outlining our assumptions for each parameter in the ionization mean free path (equation (10)).

- **Constant beam utilization efficiency η_b**: The beam utilization, inferred from the Faraday trace, has been observed to vary little (∼5%-10 %) between gases and operating conditions in both this work and [11]. We average η_b across all operating conditions and gases to estimate it as $\eta_\mathrm{b}=0.75$.
- **Constant cathode coupling voltage V_cc**: The voltage needed to extract cathode electrons, or cathode coupling voltage, is directly measured with the cathode-to-ground voltage (V_c2g) and plasma potential: $V_{cc}=|V_\mathrm{c2g}-V_\mathrm{p}|$. Experimentally, we observe this quantity to vary by $<$ 5 V across all operating conditions. We take the average of V_cc across all operating conditions and gases to estimate it as 25 V.
- **Constant length of acceleration region L_acc**: The length of the acceleration region, which determines the electric field in Ohm's law, is a non-linear function of parameters like magnetic field shape/strength, discharge voltage, and background pressure, which makes it difficult to determine *a-priori* [39, 40]. Non-invasive measurements of the acceleration region for the H9 and other similar power class magnetically shielded Hall thrusters show that the channel normalized width $\bar{L}_\mathrm{acc}=L_\mathrm{acc}/L_\mathrm{ch}$ is typically $\sim$ 7.5–17.5$\times10^{-2}$ across a range of discharge voltages, operating pressures, and gases [39–41]. Therefore, in this analysis, we average this range and make the strong assumption that it is a constant $\bar{L}_\mathrm{acc}=12.5\times10^{-2}$.
- **Electron temperature scales with discharge voltage**: To estimate the ionization rate, k_iz we must approximate the spatially averaged electron temperature $\langle T_\mathrm{e}\rangle$ across the ionization region. In Hall thrusters, electrons gain energy through Ohmic heating, which is proportional to the applied discharge voltage. Non-invasive Thomson scattering measurements show that in magnetically shielded Hall thrusters the approximate electron temperature profile is non-linear, and the peak scales as $T_\mathrm{e}=0.2V_\mathrm{d}$ [16, 42, 43]. Following the detailed analysis of [41], we assume that the spatially averaged value is $\sim1/2$ of the peak electron temperature. As a result, $\langle T_\mathrm{e}\rangle$ scales as $0.1V_\mathrm{d}$.
  We also assume that the electron temperature is independent of gas type. While non-invasive electron temperature measurements are limited, Thomson scattering measurements on a magnetically shielded Hall thruster show similar peak T_e values for xenon and krypton [42]. Therefore, we make the strong assumption that the electron temperature scaling holds for both argon and nitrogen.
- **Neutral thermal velocity scales with discharge power**: We assume the neutral population moves at the thermal velocity determined by the anode temperature T_n. As a first-order approximation of the anode temperature scaling with discharge power, we make the strong assumption that the dominant heat transfer mechanism is radiation. With this

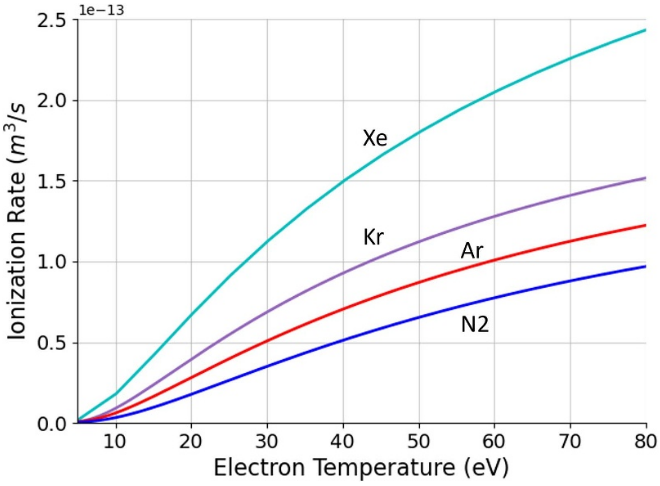

Figure 6. Ionization rate coefficient k_{iz} for xenon, krypton, argon, and nitrogen as a function of electron temperature. Cross section data is sourced from [45–47].

assumption, we can approximate the temperature scaling from a known reference temperature and power as

$$T_{\mathrm{n}} = T_{\mathrm{ref}} \left(\frac{P}{P_{\mathrm{ref}}} \right)^{\frac{1}{4}}, \tag{20}$$

where we define the reference temperature T_{ref} and power P_{ref} to be 400 ° C and 4.5 kW. These values correspond to our best estimate of the anode temperature while operating on xenon at a discharge voltage of 300 V and current of 15 A.

- **Electron collision frequency is constant and scales with the cyclotron frequency**: Per equation (5), we assume the electron collision frequency is constant and is proportional to the cyclotron frequency scaled by a constant α. This Bohm-like approximation is a common assumption made by a number of previous authors attempting to model anomalous transport [13–15, 19, 44], and has proven to be sufficient to capture key trends in the Hall thruster physics. With that being said, this scaling is an oversimplification of the highly non-linear, wave-driven transport. We note that in practice, since we operate at a single magnetic field strength, the merits of assuming Bohm-like scaling and its effects on the model predictions is not investigated. To estimate α in equation (5) , which physically represents the inverse Hall parameter, we utilize direct experimental measurements of the H9 operating on krypton presented in [16], which show $\alpha \approx 10^{-2}$.
- **Ionization rate is determined by the electron temperature**: We utilize the electron temperature in conjunction with the total ionization cross section for each species to determine the ionization rate coefficients $k_{\mathrm{iz}} = \langle v_{\mathrm{e}}(T_{\mathrm{e}})\sigma_{\mathrm{iz}} \rangle$. We plot the ionization rate coefficients for each gas in figure 6. We see that at a given electron temperature, xenon has the largest ionization rate, followed by krypton, argon, and then nitrogen. The ionization rate monotonically increases as the electrons gain more energy (higher T_{e}).

We summarize the model input parameters and their assumed values in table 3.

4.3. Model calibration

Our model for the mass utilization efficiency is a function of one free parameter $\bar{L}$, which physically represents the combined width of the ionization and acceleration region. While we are able to estimate the width of the acceleration region from non-invasive ion velocity measurements, the ionization region, which is located further upstream, is not optically accessible. As a result of the uncertainty in the ionization region width, we treat $\bar{L}$ as a free parameter to learn from the experimental data. In this analysis, we make the strong assumption that $\bar{L}$ is approximately constant across all gas types and operating conditions and learn a single value for the entire data set.

To learn $\bar{L}$ from the experimental data, we utilize similar Bayesian inference techniques to those outlined in section 4.1.2. Bayesian inference updates our prior belief in the the parameter $\bar{L}$, after introducing the experimental mass utilization data. We assume a uniform prior of the form U(0,1.25L_{ch}), which physically means that $\bar{L}$ is equally likely to take any value from 0 to 1.25L_{ch}. The upper bound on this range is motivated by experimental measurements that show that the acceleration process occurs downstream of the thruster exit plane in magnetically shielded Hall thrusters [39, 40]. Therefore, it is possible that the combined length of the acceleration and ionization zones exceeds the channel length. As with our analysis of the $E\times B$ data, we utilize Markov chain Monte Carlo to generate samples from the un-normalized posterior distribution of Bayes' rule shown in equation (16). We use these samples to estimate statistics like the mean and variance, which inform our best estimate and uncertainty of $\bar{L}$.

5. Results

We show in figure 7(a) comparison of our experimental measurements of mass utilization to model predictions as a function of the normalized inverse ionization mean free path $1/\bar{\lambda}_{\mathrm{i}}$. For each experimental measurement, we utilized the assumptions of section 4.2 to relate the global properties of the discharge, i.e. current, voltage, and gas type, to an effective ionization mean free path. We then normalize the result to the smallest mean free path in our data set. To measure the mass utilization experimentally, we employed the Faraday, $E\times B$, and Langmuir probes and associated analysis from section 3.

As shown in figure 7, the experimentally-inferred mass utilization for each gas generally improves as the ionization mean free path decreases, ultimately approaching unity with sufficiently small λ_{i}. The fact that all four disparate gases generally follow the same curve serves as an initial validation for our simplified theory for mass utilization. Physically, these trends stem from the fact that a smaller λ_{i} leads to an increasing fraction of ionized input propellant. For each propellant, the decrease in λ_{i} is primarily driven by an increase in the discharge current and thus plasma density.

Table 3. Key model assumptions of plasma parameters.

Parameter	Variable	Value
Electron temperature	T_e	$0.1V_d$ eV
Beam utilization	η_b	0.75
Cathode coupling voltage	V_{cc}	25 V
Inverse Hall parameter	α	1E-2
Acceleration region width	L_{acc}	5 mm
Reference anode temperature	T_{ref}	400° C
Reference thruster power	P_{ref}	4.5 kW
Magnetic field	B	$B_{r_{max}}$

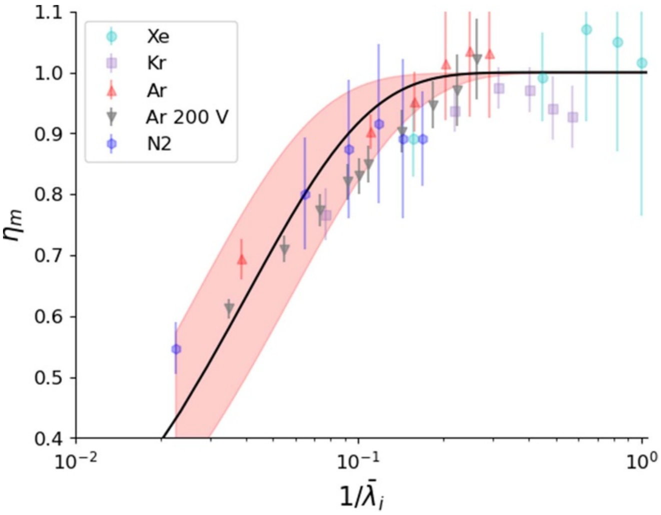

Figure 7. Experimental data and mass utilization model plotted against the normalized inverse ionization mean free path. The 95% credible intervals of the learned parameter $\bar{L}$ are plotted in red.

The experimental uncertainty in mass utilization shown in figure 7 generally increases with smaller ionization mean free path. This can be largely attributed to uncertainty in the fraction of current (Ω_s) carried by multiply charged species at these smaller mean free paths. Indeed, per the discussion in [11], higher discharge currents (and therefore smaller mean free paths per equation (10)) translate to higher production rates of multi-charged ions. As a result, our ability to identify the individual current fractions for each species suffers, yielding a higher mass utilization uncertainty. This enhanced current fraction uncertainty may also be a contributing factor to some of the values that show a mass utilization higher than unity.

Figure 7 also shows the predictions of our calibrated analytic model. To generate these trends, as outlined in section 4, we utilized Markov chain Monte Carlo to learn a probability distribution for the characteristic length $\bar{L}$. The solid line in figure 7 represents the mean of these model evaluations. We also show the 95% credible intervals as the shaded red region.

We see that our mass utilization model follows the same non-linear increase to unity as the experimental data. This is a direct result of equation (9), which shows that mass utilization monotonically increases with decreasing λ_i until all the input propellant is ionized. In general, the uncertainty in the experimental mass utilization measurements for most data points falls within the 95 % credible intervals of the model prediction. This indicates that our model follows the same trends as the data, which lends validation to our underlying assumptions. Indeed, even though we considered four propellants, the model is broadly able to represent the key trends formulated as a function of a single parameter, the inverse ionization mean free path.

As a final result, we show in figure 8 the probability distribution of the free parameter $\bar{L}$, where we have normalized the values to the channel length L_{ch}. This distribution approximately has the form of a skewed exponential distribution (Gamma, Skew-normal) centered at $\bar{L}/L_{ch} = 0.36$. The 95% credible intervals are CI[0..25,0.54].

The breadth of the distribution in figure 8 represents uncertainty in the learned characteristic length. The spread in the distribution is the result of two key factors: uncertainty in the mass utilization data, and physical changes in the ionization width due to operating condition and gas type. The uncertainty in $\bar{L}$ propagates directly into the mass utilization prediction, as indicated by the shaded red region in figure 7. At $1/\bar{\lambda}_i < 0.1$, the spread of $\bar{L}$ results in a $\pm 15\%$ variability in the mass utilization prediction. This variability in the prediction is on par with the uncertainty in the experimental data.

The mean value of this distribution, which represents our best estimate of $\bar{L}$, is qualitatively similar to that found in calibrated high fidelity simulations of this thruster [41]. Indeed, in both the simulations and this work, the combined width of the ionization and acceleration zone is $\sim$1/2 of the channel length.

In summary, we have shown that Hall thruster mass utilization over multiple operating conditions and propellants, when expressed as a function of the ionization mean free path, can be collapsed to a single curve. We further have shown that as a function of one free parameter, our simple analytical model captures the data within experimental uncertainty. We discuss in section 6 the implications of these results, including the model limitations and scaling with discharge voltage and magnetic field strength.

6. Discussion

In this section, we discuss key aspects of our findings. This includes limitations of our approach and the extensibility of

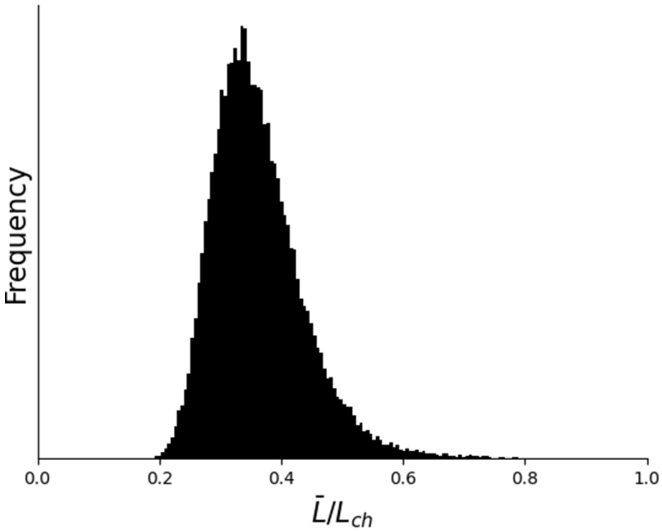

Figure 8. Histogram of samples drawn from the posterior distribution of $\bar{L}$ normalized to the thruster channel length L_{ch}.

the model to predict mass utilization trends with variable discharge voltage and magnetic field strength.

6.1. Model limitations

While our model for the mass utilization does represent the experimental data, it has some key limitations, which we discuss here. First, since the model is spatially averaged, it cannot capture the non-linear spatial variations along the discharge channel exhibited by electron temperature, plasma density, and electron collision frequency typically found in detailed thruster experiments and calibrated simulations [16, 24, 41]. However, in spite of these simplifying assumptions, the mass utilization model still largely replicates the trends in the experimental data on many different gases. Physically, this is because the spatially averaged quantities are able to capture the scaling/changes of the key parameters that drive differences in mass utilization efficiency between gases and operating conditions—plasma density, ionization rate, and neutral thermal speed.

Another key assumption we made in our model is that the ratio of mass flow rates at the anode and channel exit could be re-written in terms of the ratio of number densities at the two locations (equation (1)). While this is valid for the noble gases tested, it may not be a good approximation for gases like nitrogen that can dissociate. More accurately, the mass utilization for nitrogen should be written as

$$\eta_m = 1 - \frac{\dot{m}_{\mathrm{n}}(L_{\mathrm{ch}})}{\dot{m}_{\mathrm{n}}(0)} = 1 - \frac{n_{N_2}(L_{ch})\, m_{N_2} v_{N_2} + n_N(L_{ch})\, m_N v_N}{n_{N_2}(0)\, m_{N_2} v_{N_2}}, \tag{21}$$

where we have defined species-specific quantities with the subscripts N and N_2. While the formulation of equation (21) is more accurate, it is difficult to use in practice. This is because the neutral continuity equation for monatomic and diatomic nitrogen are coupled to each other, and cannot be easily integrated. Therefore, to keep the simplicity of the model, we ignored the monatomic species which may have affected the accuracy of the predictions. Since monatomic nitrogen has a faster thermal speed due to its lighter mass, neglecting this species would lead to an over-prediction of the mass utilization efficiency. This explanation could be one reason why at the shortest λ_{i} conditions for nitrogen shown in figure 7, the model over-predicts the mass utilization. This is in contrast to the longer λ_{i} conditions for nitrogen where the model captures the data more accurately.

Lastly, we note that there are some parameters in λ_{i} that we did not vary in this study. Namely, we did not alter the magnetic field strength, and we only investigated a narrow range of discharge voltages (200–300 V). Furthermore, all our data is from a single thruster in one electrical configuration. Therefore, the values assumed for the constants in equation (10) may be specific for this device, and could change between different magnetically shielded Hall thrusters. As a result, our conclusion that the model captures the experimental mass utilization data could be limited to the ranges tested in this work until more experimental data is gathered. The extensibility thus remains an open question. With that being said, we can analyze the model scaling with other parameters like discharge voltage by comparing to experimentally observed trends. We explore this scaling further in section 6.2.

6.2. Scaling of η_m with discharge voltage

In this study, we demonstrated that the model accurately captures the experimental data over the range of discharge voltages tested. In this section, we extend the model by parametrically varying the discharge voltage beyond the scope of the experimental data to see how the mass utilization predictions scale. We fix the discharge current to 15 A for this analysis and utilize the same assumptions described in section 4 for the remaining parameters in λ_{i}. In figure 9, we plot the mass utilization prediction with discharge voltage for xenon, krypton, argon, and nitrogen.

The mass utilization prediction for each species with discharge voltage follows a similar non-monotonic trend. We first see an increase in mass utilization with discharge voltage followed by a decrease. This non-monotonic behavior has been observed previously on many different Hall thrusters operating on xenon with increasing discharge voltage at a fixed discharge current or mass flow rate [32, 33, 48]. This trend in the mass utilization can be explained by our formulation of the ionization mean free path (equation (10)), which we re-write here in terms of parameters that vary with discharge voltage as

$$\lambda_{\mathrm{i}} \propto \frac{V_{\mathrm{d}}\sqrt{T_{\mathrm{n}}}}{k_{\mathrm{iz}}(T_{\mathrm{e}})},\ T_{\mathrm{e}} = 0.1 V_{\mathrm{d}}. \tag{22}$$

Notably, in this formulation we can see that the ionization mean free path is a balance between the discharge voltage and neutral temperature against the ionization rate. A higher discharge voltage leads to more electron cross field transport

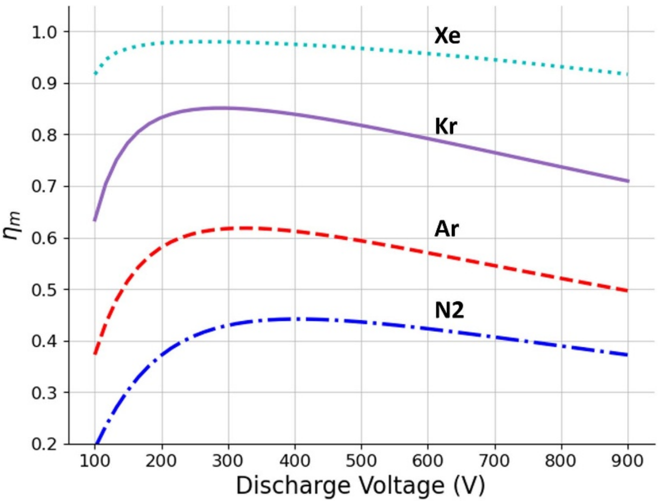

Figure 9. Mass utilization efficiency model predictions as a function of discharge voltage for different gas species.

and thus lower channel plasma density. The neutral temperature grows with discharge voltage as well per equation (20), due to enhanced power deposition to the anode. These two effects serve to increase the ionization mean free path and decrease ionization. This is balanced by the ionization rate, which increases monotonically with discharge voltage (hotter T_e). In the context of figure 6, we see that there is a sharp increase in the ionization rate for all gases between 10 and 20 eV. This stronger dependence dominates the mean free path at lower voltages, which corresponds in figure 9 to the rise in mass utilization with voltage at lower values (100–200 V). At higher V_d, the ionization rate grows more slowly than the discharge voltage and neutral thermal temperature, leading to a decrease in the mass utilization. As a result of these effects, we see the non-monotonic behavior shown in figure 9, with a predicted peak in mass utilization at 200–400 V.

While figure 9 does capture the general trends exhibited by experimental data, detailed acceleration region measurements have shown a broadening in the width L_{acc} with increasing discharge voltage [40]. Therefore, our assumption that L_{acc} is a constant over the entire discharge voltage range from 100–900 V is likely an oversimplification. Per equations (8) and (10), an increase in the acceleration region width leads to lower electric fields, promoting higher average electron densities and more ionization. As a result, in practice, the mass utilization may not decrease as precipitously as shown in figure 9 at high discharge voltages.

Ultimately, the fact that our model captures observed experimental trends of mass utilization with discharge voltage ([32, 33, 48, 49]), at least qualitatively, suggests that our model provides a plausible explanation for the underlying physics driving mass utilization. Additional validation would require direct experimental mass utilization data for each gas at higher discharge voltages.

7. Conclusion

Hall thruster mass utilization, which is a key driver of device efficiency, historically suffers for non-conventional, more difficult to ionize gases. In order to elucidate the underlying physics that govern mass utilization, we have proposed, in this work, a first principles scaling law for the physical processes that drive ionization on disparate gases. The analytic model is derived by integrating the neutral continuity equation along the length of the thruster channel. The result is a simple scaling law that relates the combined width of the Hall thruster ionization and acceleration regions, termed the characteristic length, to the ionization mean free path for each operating condition. To validate the model, we collected mass utilization data on a magnetically shielded Hall thruster operating on various propellants. This includes data from previous campaigns on xenon and krypton and new data collected on argon and nitrogen. On each propellant, we parametrically varied the ionization mean free path and inferred the mass utilization with a suite of far-field probes.

The results indicate that with a learned characteristic length for the entire data set, the model accurately captures the trends in mass utilization as a function of the ionization mean free path for each gas. This suggests that our model may be capturing some of the underlying physics that drive ionization in magnetically shielded Hall thrusters. To further test our formulation, we explored the model predictions outside the range of experimental data. We demonstrated that the model is consistent with the observed non-monotonic scaling of mass utilization with discharge voltage seen in other Hall thrusters. Given the accuracy of the scaling law over a wide range of experimental data, this model could be a beneficial tool for understanding the driving processes that influence mass utilization of thrusters operating on disparate propellants.

Data availability statement

The data cannot be made publicly available upon publication due to legal restrictions preventing unrestricted public distribution. The data that support the findings of this study are available upon reasonable request from the authors.

Acknowledgments

This work was supported by a NASA Space Technology Graduate Research Opportunity (80NSSC23K1187). The authors would also like to thank Leanne Su, Parker Roberts, Madison Allen, Chris Sercel, Tate Gill, Collin Whittaker, Eric Viges, and Thomas Marks for help with thruster setup and testing.

Appendix

We correct the Faraday probe trace for extra current collected between the guard ring and collector with the correction factor κ_G defined as

$$\kappa_G = \pi\left(R_{GR}^2 - R_C^2\right)\frac{2\pi R_c h_c}{2\pi R_c h_c + 2\pi R_{GR} h_{GR}}, \qquad (23)$$

where R_c, h_c, R_{GR}, and h_{GR} are the heights and radii of the collector and guard ring. Additionally, a correction factor must be applied to account for SEE from the probe due to ion impact. This factor, κ_{SEE}, is defined as

$$\kappa_{SEE} = \frac{1}{1+\sum_i \frac{\Omega_i \gamma_i}{Z_i}}. \qquad (24)$$

The SEE yield γ_i for each ion species was taken from [50–52].

ORCID iDs

W J Hurley https://orcid.org/0009-0005-7666-625X
B A Jorns https://orcid.org/0000-0001-9296-2044

References

[1] Goebel D and Katz I 2008 *Fundamentals of Electric Propulsion: Ion and Hall Thrusters* (Wiley)
[2] Unfried K G, Cassady J R, Hoskins A W and Marschke J D 2024 Electric propulsion propellant considerations: Can we still use xenon and krypton *38th Int. Electric Propulsion Conf.*
[3] Abbasrezaee P and Saraaeb A 2021 *J. Aerosp. Technol. Manage.* **13** e1521
[4] Oleson S R *et al* 2021 Compass final report: Nuclear electric propulsion (nep)-chemical vehicle 1.2 *Technical Report*
[5] Foust J 2023 Spacex launches first upgraded starlink satellites (available at: https://spacenews.com/spacex-launches-first-upgraded-starlink-satellites) (Accessed 14 June 2024)
[6] Andreussi T, Ferrato E and Giannetti V 2022 *J. Electr. Propul.* **1** 31
[7] Su L and Jorns B 2021 *J. Appl. Phys.* **130** 163306
[8] Marchioni F and Cappelli M A 2021 *J. Appl. Phys.* **130** 053306
[9] Raitses Y and Ashkenazy J 1996 Discharge characteristics of hall current accelerators *Proc. 17th Int. Symp. on Discharges and Electrical Insulation in Vacuum* vol 1 pp 492–6
[10] Cohen-Zur A, Gany A, Fruchtman A and Ashkenazy J 2000 Channel length and wall recombination effects in the hall thruster *36th AIAA/ASME/SAE/ASEE Joint Propulsion Conf. and Exhibit* p 3654
[11] Su L L, Roberts P J, Gill T M, Hurley W J, Marks T A, Sercel C L, Allen M G, Whittaker C B, Viges E and Jorns B A 2024 *J. Propul. Power* **40** 661–800
[12] Reid B M and Gallimore A D 2007 Review of hall thruster neutral flow dynamics *30th Int. Electric Propulsion Conf.*
[13] Jorns B 2018 *Plasma Sources Sci. Technol.* **27** 104007
[14] Marks T A and Jorns B A 2023 *Plasma Sources Sci. Technol.* **32** 045016
[15] Mikellides I G and Ortega A L 2019 *Plasma Sources Sci. Technol.* **28** 014003
[16] Roberts P J and Jorns B A 2024 *Phys. Rev. Lett.* **132** 135301
[17] Brown Z A and Jorns B A 2023 *Phys. Rev. E* **108** 065204
[18] Fife J M 1998 Hybrid-PIC modeling and electrostatic probe survey of Hall thrusters *PhD Thesis* Massachusetts Institute of Technology
[19] Koo J W and Boyd I D 2006 *Phys. Plasmas* **13** 033501
[20] Hofer R, Katz I, Goebel D, Jameson K, Sullivan R, Johnson L and Mikellides I 2008 Efficacy of electron mobility models in hybrid-pic hall thruster simulations *44th AIAA/ASME/SAE/ASEE Joint Propulsion Conf. & Exhibit* p 4924
[21] Cusson S E, Hofer R R, Lobbia R, Jorns B A and Gallimore A D 2017 Performance of the H9 magnetically shielded Hall thrusters *35th Int. Electric Propulsion Conf.*
[22] Hofer R R, Cusson S E, Lobbia R B and Gallimore A D 2017 The H9 Magnetically Shielded Hall Thruster *35th Int. Electric Propulsion Conf.*
[23] Mikellides I G, Katz I, Hofer R R, Goebel D M, de Grys K and Mathers A 2011 *Phys. Plasmas* **18** 033501
[24] Mikellides I, Katz I, Hofer R and Goebel D 2014 *J. Appl. Phys.* **115** 043303
[25] Frieman J D *et al* 2021 Performance of the 12.5-kw advanced electric propulsion system engineering test unit hall thruster *68th JANNAF Propulsion Meeting*
[26] Su L L, Gill T M, Roberts P J, Hurley W J, Marks T, Sercel C, Allen M G, Whittacker C B, Byrne M, Brown Z, Viges E and Jorns B 2023 *SciTech Forum and Exposition*
[27] Peterson P Y, Kamhawi H, Huang W, Williams G, Gilland J H, Yim J, Hofer R R and Herman D A 2016 Nasa's Hermes hall thruster electrical configuration characterization *52nd AIAA/SAE/ASEE Joint Propulsion Conf.* p 5027
[28] Hruby V, Hohman K and Szabo J 2022 Air breathing hall effect thruster design studies and experiments *37th Int. Electric Propulsion Conf.*
[29] Neumann A, Hannemann K and Brchnelova M 2019 Challenges of cryopumping ep-propellants in dlr's electric propulsion test facility *36th Int. Electric Propulsion Conf.*
[30] Lobbia R B and Beal B E 2017 *J. Propul. Power* **33** 566–81
[31] Brown D L, Walker M L, Szabo J, Huang W and Foster J E 2017 *J. Propul. Power* **33** 582–613
[32] Huang W, Shastry R, Soulas G C and Kamhawi H 2013 Farfield Plume Measurement and Analysis on the NASA-300M and NASA-300MS *33rd Int. Electric Propulsion Conf.*
[33] Hofer R R and Gallimore A D 2006 *J. Propul. Power* **22** 732–40
[34] Huang W and Shastry R 2015 *Rev. Sci. Instrum.* **86** 073502
[35] Shastry R, Hofer R R, Reid B M and Gallimore A D 2009 *Rev. Sci. Instrum.* **80** 063502
[36] Stebbings R, Turner B R and Smith A 1963 *J. Chem. Phys.* **38** 2277–9
[37] Hause M L, Prince B D and Bemish R J 2013 *J. Appl. Phys.* **113** 163301
[38] Miller J S, Pullins S H and Levandier D J 2002 Chiu Y h and Dressler R A 2002 *J. Appl. Phys.* **91** 984–91
[39] Cusson S E, Dale E T, Jorns B A and Gallimore A D 2019 *Phys. Plasmas* **26** 023506
[40] Chaplin V H, Jorns B A, Lopez Ortega A, Mikellides I G, Conversano R W, Lobbia R B and Hofer R R 2018 *J. Appl. Phys.* **124** 183302
[41] Su L L, Marks T A and Jorns B A 2024 *Plasma Sources Sci. Technol.* **33** 065008
[42] Roberts P J, Allen M G, Brick D G and Jorns B A 2024 Empirical closures for momentum and energy transport in hall thrusters based on thomson scattering measurements *38th Int. Electric Propulsion Conf. (Electric Rocket Society, Toulouse, 2024)*
[43] Vincent B, Tsikata S and Mazouffre S 2020 *Plasma Sources Sci. Technol.* **29** 035015
[44] Boeuf J P 2017 *J. Appl. Phys.* **121** 011101

[45] Dragnea H C, Ortega A L, Kamhawi H and Boyd I D 2020 *J. Propul. Power* **36** 335–45

[46] Straub H, Renault P, Lindsay B, Smith K and Stebbings R 1995 *Phys. Rev. A* **52** 1115

[47] Straub H, Renault P, Lindsay B, Smith K and Stebbings R 1996 *Phys. Rev. A* **54** 2146

[48] Hall S J, Jorns B A, Gallimore A D, Kamhawi H and Huang W 2022 *J. Propul. Power* **38** 97–110

[49] Hofer R 2004 Development and Charachterization of High-Efficiency, High-Specific Impulse Xenon Hall Thrusters *PhD Thesis* University of Michigan Ann Arbor, MI

[50] Hagstrum H D 1954 *Phys. Rev.* **96** 325

[51] Hagstrum H D 1956 *Phys. Rev.* **104** 672

[52] Mahadevan P, Magnuson G, Layton J and Carlston C 1965 *Phys. Rev.* **140** A1407